



Cite this: *Nanoscale Adv.*, 2025, 7, 6196

## Beyond application-specific design: a generalized deep learning framework for optical property prediction in $\text{TiO}_2/\text{GaN}$ nanophotonic metasurfaces

Adrita Anwar,<sup>a</sup> Shahamat Mustavi Tasin,<sup>ab</sup> Mahabub Alam Bhuiyan,<sup>c</sup> Nymul Yeachin,<sup>cd</sup> Sharnali Islam <sup>a</sup> and Khaleda Ali <sup>a\*</sup>

Metalenses have garnered significant attention for their remarkable ability to precisely focus light while obviating the inconvenience and intricacy associated with conventional curved lenses. Identifying the best response for these phase gradient optical devices necessitates intensive trial and error analysis of meta-atoms with various shapes, materials and dimensions. In this work, we present an artificial intelligence-based framework to predict the highly skewed, complex transmission and phase responses of the constituent nanorods. Here, we employed a transfer learning model to train on two extensive datasets comprising the optical responses of gallium nitride and titanium dioxide nanopillars, each integrated onto silica substrates. The accuracy of the dataset was assessed through experimental investigation, particularly inspecting transmittance and the refractive index for a  $\text{TiO}_2$  layer of a certain height. A reasonable agreement has been obtained for both cases. The optimized algorithm estimates the performance in terms of amplitude and phase, attaining minimum Mean Squared Error (MSE) values of  $2.3 \times 10^{-6}$  and  $1.31 \times 10^{-5}$ , respectively, for a wavelength range of 600–700 nm. To validate the effectiveness of our proposed approach, focusing performance was exhibited for two flat lenses: a smaller lens with a 20  $\mu\text{m}$  diameter and a larger lens featuring an identical diameter and focal length of 100  $\mu\text{m}$ . A brief study on the effects of varying angles of incident light has also been conducted. While minimizing the need for typically tedious and at times ineffective repetitive analyses, the parameterized datasets can be beneficial for developing different optical components.

Received 4th June 2025

Accepted 6th August 2025

DOI: 10.1039/d5na00550g

[rsc.li/nanoscale-advances](http://rsc.li/nanoscale-advances)

## 1 Introduction

Metalenses, employing nanoscale structures to manipulate light at the sub-wavelength level, offer great potential for the development of versatile and efficient optical devices.<sup>1,2</sup> Unlike conventional bulky lenses that require longer optical paths, these considerably thinner and lighter elements possess the competence to alter intensity, phase, and time varying the E-field orientation of incident beams.<sup>3–7</sup> Additionally, they can readily be tailored to suppress optical aberrations and hence ensure sharper focusing.<sup>8–10</sup> In consequence, such flat lenses, today, have unveiled immense possibilities, ranging from sensing<sup>11</sup> and high resolution imaging<sup>12</sup> to augmented reality.<sup>13</sup>

To address the demands of diverse applications, existing literature emphasizes using different geometric configurations, materials, and meta-atom orientation angles in metalens designs.<sup>14,15</sup> To perform chiral imaging, Sun *et al.*<sup>16</sup> experimentally demonstrated 3D plasmonic metalens based on gold and anisotropic polymethyl methacrylate elliptical nanopillars. In ref. 14, planar lenses suited for chromatic holographic operations were realized by etching nanoholes of uniform diameters onto a silver film. Metallic flat lenses, however, have limited optical field manipulation due to absorption losses. Also, designs with apertures, wherein light must traverse longer routes, exacerbate this constraint.<sup>12</sup>

Dielectric materials with high refractive indices ( $n > 2$ ) and low absorption are preferable in this context.<sup>17</sup> In ref. 18, the demonstration of a dielectric metalens, operating at three distinct wavelengths represents one of the pioneering advances in the relevant research field. Recently, structures with quasi-continuous nanofins or rectangular strips have been incorporated to showcase broadband and highly efficient performance at different spectra.<sup>19,20</sup> Barulin *et al.* in ref. 21 introduced a dielectric planar lens that allows light to be captured from

<sup>a</sup>Department of Electrical and Electronic Engineering (EEE), University of Dhaka (DU), Dhaka 1000, Bangladesh. E-mail: [khaleda.eee@du.ac.bd](mailto:khaleda.eee@du.ac.bd)

<sup>b</sup>Department of Mechanical and Aerospace Engineering, University of Central Florida, Orlando, Florida 32816, USA

<sup>c</sup>Department of Physics, University of Dhaka, Dhaka 1000, Bangladesh

<sup>d</sup>School of Physics, Applied Physics and Astronomy, Rensselaer Polytechnic Institute, Troy, NY 12180, USA



fluorescent sources of two distinct wavelengths. Regardless of the functionality of these flat lenses, two criteria must be universally satisfied: attaining high optical transmittance and ensuring full phase mapping in the range of 0 to  $2\pi$ .

Achieving the desired phase modulation with enhanced light throughput necessitates a meticulous and iterative optimization process, often characterized by trial-and-error experimentation. It is worth noting that despite conducting these stringent adjustment procedures, the performance metrics of the flat lens are effectively calibrated only for certain materials, within a limited wavelength range, and for a restricted array of

applications. Systematic adoption of different AI algorithms would be advantageous to minimize the design timeline and escalated costs associated with traditional design approaches.<sup>22-28</sup>

Studies reported in ref. 23 and 24 utilize simulated datasets and reveal the efficacy of DNN in predicting the optical responses throughout various regions of the visible spectrum. However, models trained solely on unvalidated simulated results may exhibit poor generalizability owing to unaccounted fabrication-induced discrepancies. While inverse design techniques aid in ascertaining the appropriate phase and

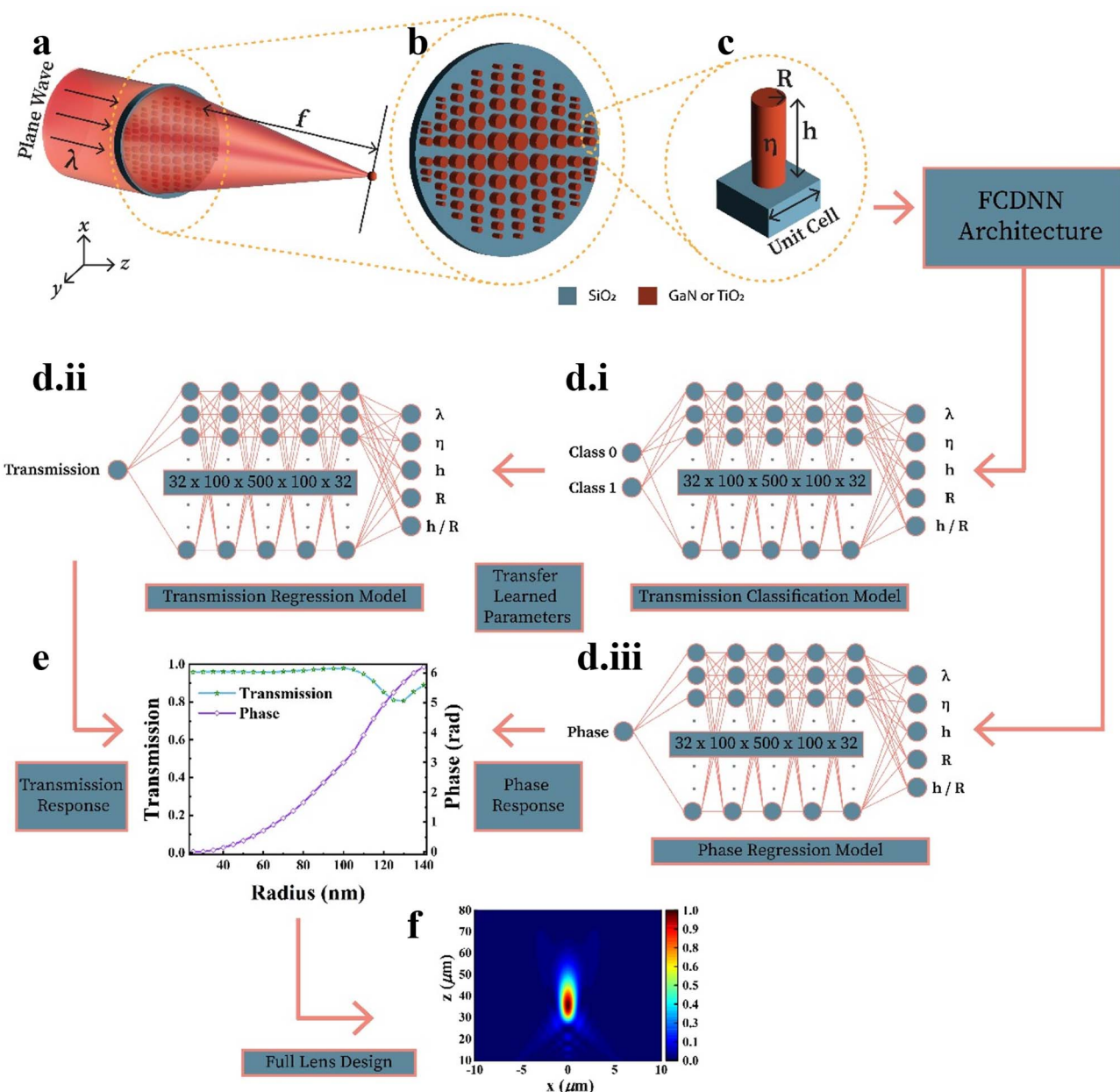


Fig. 1 Our design framework. (a) Three-dimensional schematic structure of a metalens: a plane wave is normally incident on an array of circular nanorods, and then the incident light is focused at focal length  $f$ . (b) The building blocks of a metalens are nanopillars composed of GaN/TiO<sub>2</sub> on a SiO<sub>2</sub> substrate. (c) Unit cell of the metalens with nanorods of height  $h$ , diameter  $D$  and refractive index  $\eta$ . (d(i-iii)) The FCDNN architecture is shown for the transmission and phase model. (e) Predicted transmission and phase allocation as a function of radius. (f) Intensity profile for the designed full metalens.

transmission profiles necessary for obtaining the desired device geometries, they also inherently rely on precise forward models for effective optimization.<sup>25–27</sup> As evident by these state-of-the-art research studies, the existing architectures are typically trained to represent a unique geometric arrangement or constrained operating window. Alternatively, hybrid means combining deep learning with evolutionary algorithms—such as genetic algorithms or particle swarm optimization<sup>7,29,30</sup>—have been explored to enhance design flexibility. Nevertheless, such methods are computationally intensive, and for nonlinear distributions, may converge to solutions that are theoretically optimal yet realistically unfeasible, not to mention that their performance depends on high-fidelity datasets generated through forward modeling. The accuracy and authenticity of the training data, therefore, remain essential, highlighting the vital importance of robust forward modeling practices in metalens design. Additionally, a significant technical hurdle emerges from the highly skewed transmission spectral distribution, where high-transmission data substantially outnumber low-transmission data.

This work overcomes the aforementioned challenge by presenting two distinct data libraries of optical responses for  $\text{TiO}_2$ –GaN-based nanopillars operating in the 600–700 nm spectrum. While previous studies<sup>31–34</sup> have applied machine learning to specific metasurface functionalities with limited datasets and materials, we propose a broad dataset capturing both transmission and phase responses suitable for versatile applications. The validity of these datasets was subsequently confirmed through comparative analysis with lithographically fabricated  $\text{TiO}_2$  thin films. A fully connected deep neural network (FCDNN) was developed to accurately predict the highly asymmetric and complex transmission-phase responses of both structures, with rigorous multilayer benchmarking validating model efficacy. Adopting such a unified model trained on diverse datasets aids to improve the network's capacity to generalize material-specific effects under similar conditions. A full lens simulation was subsequently conducted to showcase its practical usability. The response of a full lens for varying incident angles has also been explored. The capability demonstrated through the successful design and validation of the metalens confirms the model's potential for driving inverse design.

## 2 Proposed methodology

### 2.1 Metalens design and dataset generation

The electromagnetic (EM) models of two metalenses (see Fig. 1(a) and (b)) are first constructed using two different unit cells: one comprising  $\text{TiO}_2$  nanopillars and the other consisting of GaN-based equivalents. Each structure (as in Fig. 1(c)) independently engineered on a transparent  $\text{SiO}_2$  substrate, maintains cylindrical geometry and polarization insensitivity. Such material variants are chosen since they ensure broad transparency windows, minimized absorption losses and strong light confinement while exhibiting high refractive indices.<sup>35,36</sup> In the designed device, for a certain height of nanorods, diameters are systematically varied to ensure a diffraction-limited spot. To this aim, the spherical phase profile  $\varphi(x, y)$  of a metalens that

focuses a normally incident plane wave of wavelength  $\lambda$  can be estimated as:

$$\varphi(x, y) = \frac{2\pi}{\lambda} \left( f - \sqrt{f^2 + x_p^2 + y_p^2} \right) \quad (1)$$

where  $x_p$  and  $y_p$  indicate the radial coordinates and  $f$  is the focal length. Our overall workflow is illustrated in Fig. 1.

To generate the dataset, design parameters such as height ( $h$ ), radius ( $R$ ), refractive index ( $\eta$ ) and wavelength ( $\lambda$ ) are varied and optimized to create a library of phase and transmission responses. The nanopillar heights for GaN range from 500 to 600 nm, with diameters ranging from 50 to 300 nm. However, the corresponding dimensions for  $\text{TiO}_2$  are 610–700 nm in height and 100–360 nm in diameter. With a uniform 10 nm increment for height and diameter shifts for GaN and  $\text{TiO}_2$  nanostructures, the excitation wavelength range of 600–700 nm yields 28 886 and 27 270 unique configurations for GaN and  $\text{TiO}_2$ , respectively. Each simulation set employs normally incident plane waves of discrete wavelengths on periodic unit cells. All the numerical investigations are conducted using the commercial full-wave EM solver Lumerical. Here, the phase phenomenon has a symmetric normal distribution, in contrast to the asymmetric left-skewed distribution observed in transmission characteristics (see Fig. 2).

### 2.2 Data preprocessing

As depicted in Fig. 3(a–c), the phase responses for GaN and  $\text{TiO}_2$  nanorods with different radii at various wavelengths exhibit damped variations. These sharp dips correspond to the coupling of the incident light with the surface mode of the periodic lattice.<sup>37</sup> Additionally, for  $\text{TiO}_2$ , the smaller dips, seen for all four wavelengths can be attributed to a higher-order resonance within the nanopillars in adjacent unit cells.<sup>38,39</sup> Since nanopillars can be thought of as Fabry–Perot resonators with low-quality factors, these mutual interferences can be ignored to capture the general trend of the phase plot for varying radii.<sup>37,40</sup> Therefore, preprocessing steps are carried out for the phase property. Such noise removal can be implemented by nonparametric smoothing techniques, including LOWESS

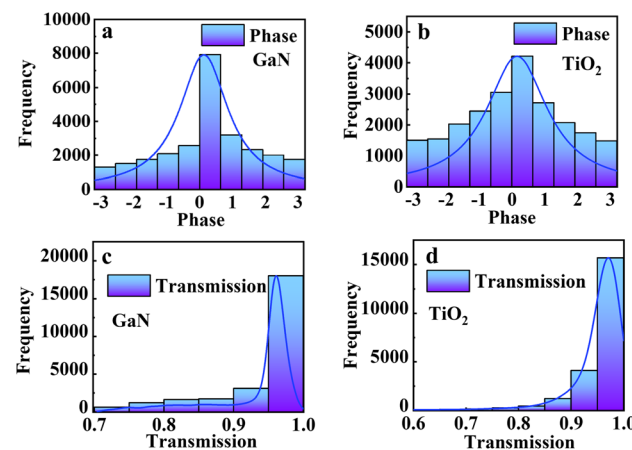


Fig. 2 (a and b) Phase and (c and d) transmission data for GaN and  $\text{TiO}_2$ .



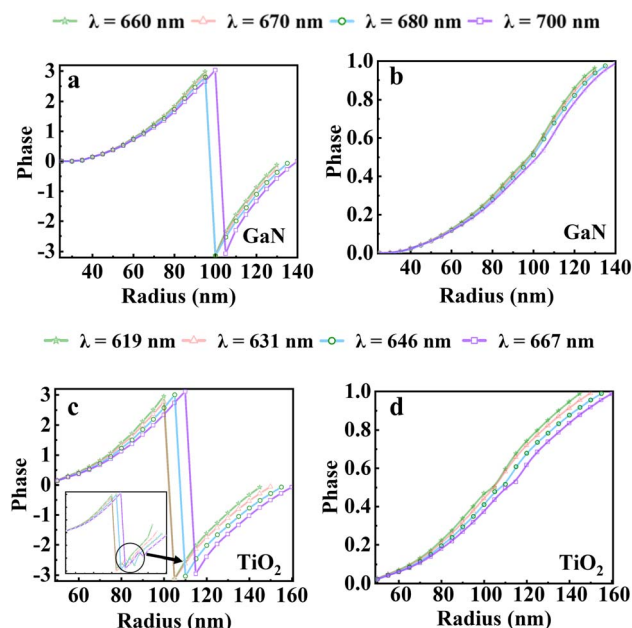


Fig. 3 Phase response (a and c) after filtering, with the inset of (c) showing damped variations. (b and d) After normalization.

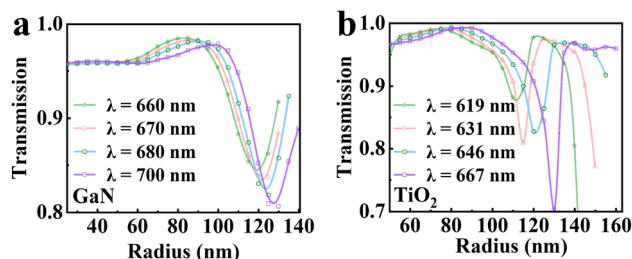


Fig. 4 Transmission after filtering for (a) GaN and (b) TiO<sub>2</sub>.

smoothing<sup>41</sup> and the bootstrap method.<sup>42</sup> In this work, LOWESS smoothing was applied to the data (Fig. 3(a–c)) due to its ability to handle outliers effectively and capability to detect complex relationships between variables.<sup>43</sup> Furthermore, the phase data were normalized to a range of 0 to 1, and any phase repetition was eliminated, as shown in Fig. 3(b and d). The transmission response for nanopillars with GaN and TiO<sub>2</sub>, processed using a Gaussian filter, is shown in Fig. 4(a) and (b), respectively. Prior to training, feature scaling was applied to the data using Scikit-Learn's<sup>44</sup> StandardScaler to standardize it so that the deep learning models utilize the data efficiently. Once all the data preprocessing steps were completed for GaN and TiO<sub>2</sub>, the datasets utilized to train the models had a total of 26 327 and 25 301 data samples, respectively.

### 2.3 Model architecture and the prediction methodology

In this section, a fully connected deep neural network (FCDNN) (as in Fig. 1(d)) has been implemented in order to accurately predict the phase and transmission behavior required for full metalens designs. Here, a common neural network comprising five hidden layers with 32, 100, 500, 100 and 32 neurons is

utilized to foresee the optical responses of both GaN and TiO<sub>2</sub> nanopillars, respectively. Such a framework demonstrates the robustness of the architecture in handling diverse datasets without compromising computational efficiency. Therefore, a transfer learning strategy is utilized to address data scarcity and reduce inherent biases in predictive modeling. While alternative techniques, such as resampling<sup>45</sup> and physics-informed models,<sup>46</sup> could be explored, our focus was on maintaining architectural simplicity and computational efficiency. Here, two transmission networks are employed, one dedicated to classification and the other to perform regression.<sup>47,48</sup> The essentiality for enhanced transmittance in flat metalenses leads to a skewed dataset, with low-transmission samples being greatly underrepresented.

At first, in the binary classification problem, transmission values less than 0.8 are assigned as class 0 (low transmission), and the rest are identified as class 1 (high transmission). The model undergoes training for 100 iterations with early stopping and the weights or the low level features from this model are later fed to the transmission regression architecture. These weights have been kept frozen for ten epochs, so that the new regression model can have reasonable output weights. After completing the ten epochs, these coefficients are unfrozen so that the new model can tweak the weights. Preemptive termination has also been employed in the transmission regression model after 500 epochs. Such a procedure improves the performance of the regression task by drawing upon the knowledge acquired from the classification job. As seen in Fig. 1(d(iii)), the phase regression model has been implemented without the use of transfer learning. For the phase regression model, training parameters have been kept consistent with those of the transmission regression representation. In both classification and regression models, the Rectified Linear Unit (ReLU)<sup>49</sup> activation function is employed in the hidden layers to introduce nonlinearity, while the initialization strategy is utilized to randomly activate the connection weights. This combination is adopted because of its computational efficiency. In the case of output layers, the sigmoid/logistic activation function<sup>50,51</sup> is utilized instead of the conventional gradient descent optimizer.<sup>52</sup> Hyperparameters such as the learning rate and batch size have been optimized for both transmission and phase paradigms. The entire training process is executed on Google Colab.<sup>53</sup> For the transmission classification task, binary cross-entropy is used as the loss function, whereas accuracy, precision and recall metrics have been considered for performance evaluation. For the transmission regression model, the Mean Absolute Error (MAE) (as defined in eqn (2)) has been employed as the loss function due to its robustness to outliers, even though the use of another loss function Mean Square Error (MSE) (see eqn (3)) leads to a more significant reduction in loss.

$$\text{MAE} = \frac{1}{n} \sum_{i=1}^n |y_i - \hat{y}_i| \quad (2)$$

$$\text{MSE} = \frac{1}{n} \sum_{i=1}^n (y_i - \hat{y}_i)^2 \quad (3)$$



where  $n$  represents the total number of training data points,  $y_i$  denotes the ground truth values, and  $\hat{y}_i$  indicates the predicted values.

### 3 Results and discussion

In this section, comprehensive multi-layer evaluations have been conducted to rigorously assess the performance of the proposed phase and transmission models for GaN and  $\text{TiO}_2$  based metaleenses. Following the validation of the effectiveness of the models, a complete lens simulation is performed, and the corresponding optical properties are examined for further in-depth analysis.

#### 3.1 Model evaluation

As part of the first stage of our evaluation, datasets within the relevant wavelength range of 600–700 nm have been systematically subjected to the Leave-One-Height-Out Cross-Validation (LOHOCV) method. The datasets for GaN, consisting of eleven distinct heights, and for  $\text{TiO}_2$ , comprising ten, have been divided into the corresponding test subsets, each representing a specific height and its associated data points. This division facilitated the structured application of the LOHOCV method, where the models have been trained on all segments except one. The remaining segment is used as the test set during each iteration. For instance, in the case of  $\text{TiO}_2$ , this process has been repeated ten times. Here, each height-specific section has been employed as a test set exactly once, ensuring a comprehensive evaluation across the entire dataset. Additionally, a validation set comprising 5% of the training data has been retained in each iteration to monitor the model's performance throughout training. This cross-validation technique provides a more robust assessment compared to the conventional train/test split, which is prone to issues such as high variance and the risk of underfitting or overfitting.<sup>54</sup> The performance of the phase and transmission models (as illustrated in Fig. 5) for both materials has been evaluated using four key metrics: Mean Squared Error (MSE), Mean Absolute Error (MAE), Root Mean Squared Error (RMSE), and  $R^2$  values.

It is observed that for GaN, even the maximum MAE and MSE achieved by the transmission and phase networks are  $3.91 \times 10^{-3}$  and  $7.28 \times 10^{-5}$ , respectively. In comparison, for  $\text{TiO}_2$ , the same properties are  $11.44 \times 10^{-3}$  and  $13.21 \times 10^{-5}$ , respectively. While both models demonstrate satisfactory performance, the overall prediction performance for GaN is notably

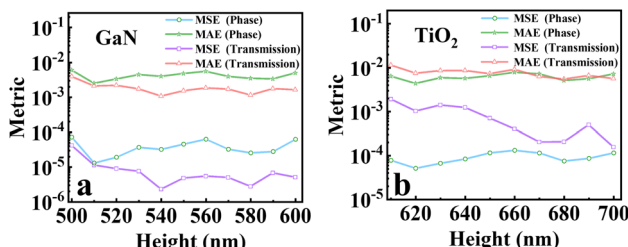


Fig. 5 Leave-one-height-out-cross-validation results for phase and transmission models for (a) GaN and (b)  $\text{TiO}_2$ .

higher than that for  $\text{TiO}_2$ . The LOHOCV evaluation results highlight the strong predictive power and accuracy of the proposed models, indicating their potential for designing metaleenses with desired properties for both GaN and  $\text{TiO}_2$ .

In the second part of the robustness profiling, data corresponding to a specific wavelength and height that meet the criteria for metalens design have been selected as test sets for both GaN and  $\text{TiO}_2$ . Predictions have been generated using the FCDNN architecture for these test sets, allowing for the construction of full metaleenses based on the predicted values. The selected heights and wavelengths are 600 nm and 700 nm for GaN, and 660 nm and 646 nm for  $\text{TiO}_2$ , respectively. Next, learning curves that depict training and validation losses have been plotted, and comparisons between FDTD simulated data and FCDNN predicted data are reported. Fig. 6 demonstrates

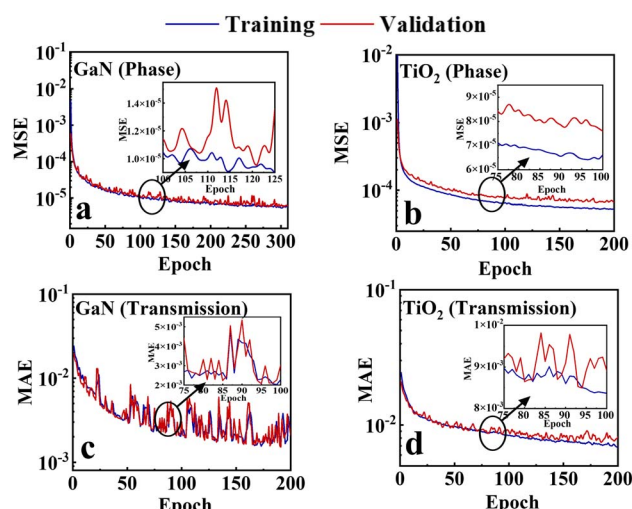


Fig. 6 Learning curves of phase (a and b) and transmission (c and d) models for GaN and  $\text{TiO}_2$ , respectively.

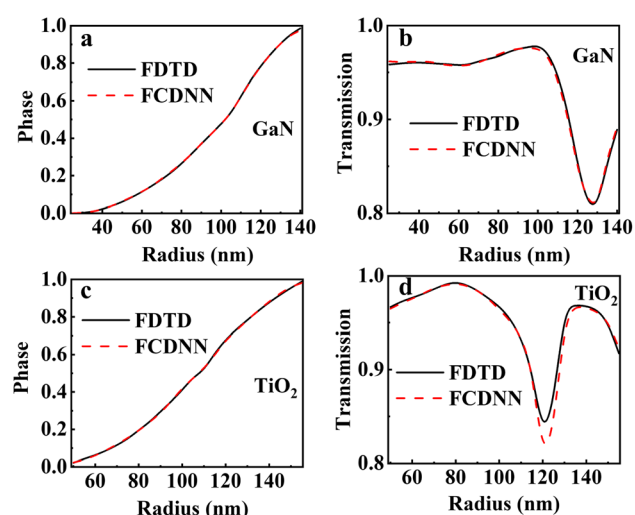


Fig. 7 Comparison between simulated (FDTD) and predicted (FCDNN) phase (a and c) and transmission (b and d) responses for GaN and  $\text{TiO}_2$ , respectively.



that both the training and validation losses decrease and level off eventually. Comparison between the FDTD simulations and the FCDNN model predictions for phase and transmission (Fig. 7) exhibits a strong alignment, indicating that they can be employed in full lens design. It is worth mentioning that the entire time for training and prediction for both the phase and transmission models is about 152 minutes, compared to 86 658 minutes of simulation using FDTD.

### 3.2 Experimental investigation

This section details the experimental deposition of  $\text{TiO}_2$  thin films and their subsequent transmittance and refractive index measurements for benchmarking the consistency and reliability of the numerically obtained dataset.

**3.2.1 Sample preparation.** A  $\text{TiO}_2$  thin film was prepared using the spray pyrolysis deposition technique as shown in Fig. 8.

In brief, an appropriate amount of titanium(iv) butoxide (purity-97%, Sigma-Aldrich) precursor and de-ionized water were taken in a beaker and stirred at 300 rpm for 30 minutes under atmospheric conditions. When the precursor was completely dissolved and the mixture became homogeneous, it was then transferred to the spray nozzle of an atomizer *via* a simple medical saline tube. Meanwhile, an ultrasonically cleaned glass substrate was placed onto a heater, which provided a constant heating temperature. When the heating temperature reached 400 °C and became stable, then the spray pyrolysis of  $\text{TiO}_2$  solution was performed using the spray nozzle with the aid of pressurized air flow, maintaining a constant flow rate of 1 ml min<sup>-1</sup>. To obtain the  $\text{TiO}_2$  layered film, the deposition was continued for 5 minutes and the spray nozzle to substrate height was kept at 25 cm throughout the deposition process.

**3.2.2 Optical measurements.** The UV-vis spectra of the fabricated  $\text{TiO}_2$  thin film were recorded within the 350 nm to 800 nm range using a UV-2600i spectrophotometer equipped with an ISR-2600Plus integrating sphere attachment. Subsequently, transmittance was computed from the acquired data

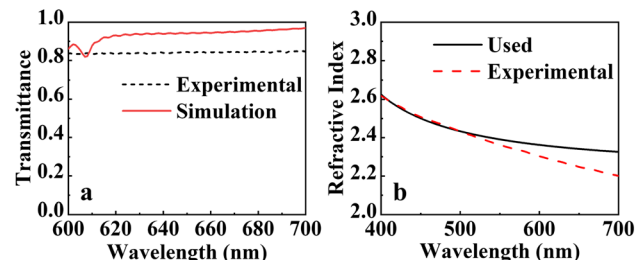


Fig. 9 (a) Experimental and simulated transmittance spectra and (b) used and experimental refractive indices of the  $\text{TiO}_2$  thin film as a function of wavelength.

based on the principle of energy conservation relation,  $A + T + R = 1$ . From these studies, transmittance spectra were compared with the simulation and plotted in Fig. 9(a). Furthermore, using the acquired reflectance data, the refractive index ( $n$ ) of the fabricated  $\text{TiO}_2$  layers was determined by using the following

formula:<sup>55</sup> 
$$n = \left( \frac{1+R}{1-R} \right) + \sqrt{\frac{4R}{(1-R)^2} - k^2}$$
, where  $R$  and  $k$  are

the reflectance and extinction coefficient respectively. The obtained refractive index and the one used in our dataset generation were plotted as a function of measured visible spectral wavelength and are presented in Fig. 9(b).

### 3.3 Full lens design

To achieve rigorous validation for our computational dataset, two full lenses have been designed using predicted phase and transmission outcomes. The  $\text{TiO}_2$  nanorod integrated large metalens has a diameter of 100  $\mu\text{m}$  and focal length of 100  $\mu\text{m}$ , and hence exhibits a numerical aperture (NA) of 0.44 at its design wavelength of 646 nm. Besides, the GaN meta-atom-based smaller lens with a 20  $\mu\text{m}$  diameter and 8  $\mu\text{m}$  focal length demonstrates a NA of 0.78 at the operating spectrum of 700 nm. Both the planar lenses are designed with a spherical phase profile, intended to independently focus collimated light onto desired focal spots. Once the phase vs. radius library has been derived from model predictions (Fig. 10(a)) and the target phase profile has been determined, the phase data are translated for the corresponding radius distribution for each spatial coordinate (Fig. 10(b)). During this stage, the complete construction of the lens has been achieved by positioning nanorods at precise locations to span the diameter of the metalens. The full lens simulation has been performed on a virtual machine (Amazon Web Services) with the following specifications: CPU – AMD EPYC 7571, vCPUs – 32, memory – 256 GB, clock speed – 2.5 GHz, with a total simulation time of approximately 6 hours. The FDTD simulations reveal that the phase imparted by the metalens closely matches with the target phase profile, as illustrated in Fig. 10(c). For the brevity of the paper, intensity plots generated from the simulations are provided only for the larger lens. Fig. 11 demonstrates that the constructed metalens achieves peak intensity at the designed focal length of 100  $\mu\text{m}$ , confirming its ability to focus incident light at the intended focal point. Alongside the simulated

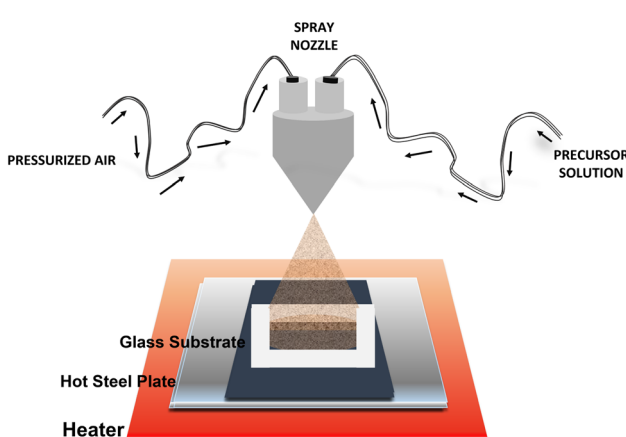


Fig. 8 Schematic diagram of  $\text{TiO}_2$  thin film deposition using a home-made spray pyrolysis.



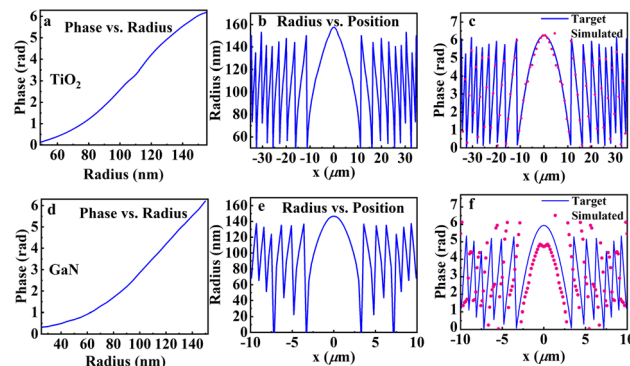


Fig. 10 Metalens design workflow: (a and d) phase vs. radius library from predicted data, (b and e) translated radius vs. position distribution and (c and f) comparison of target and simulated phase profiles.

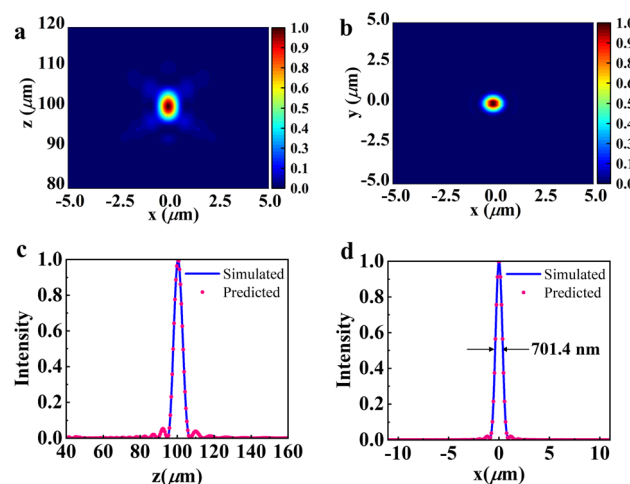


Fig. 11 Intensity profile of  $\text{TiO}_2$  based metalens (a) in the  $(x-z)$  plane and (b) in the  $(x-y)$  plane of the focal spot in the focal plane. (c) Normalized intensity distribution (simulated and predicted) at the focal point along the propagation direction ( $z$ -axis). (d) Corresponding horizontal cut at the focal spot in (b). Here, the FWHM of the focal spot is 701.4 nm.

response, the performance was also predicted using our algorithm. As expected, a strong agreement was observed between the two.

According to Abbe's diffraction limit, the minimum resolution for the designed 100  $\mu\text{m}$  metalens is calculated as  $d = \frac{\lambda}{\text{NA}} = 722.25$  nm. However, the full width at half maximum (FWHM) at the focal plane is approximately 701.4 nm, indicating that the metalens achieves sub-diffraction resolution, thereby surpassing the diffraction limit. The focusing efficiency is approximately 66.33% compared to 59.8% for the GaN-based lens.

### 3.4 Functionality assessment across angles

While our design was optimized for normal incidence conditions, we systematically evaluated the lens's performance under oblique illumination to quantify the angular tolerance and

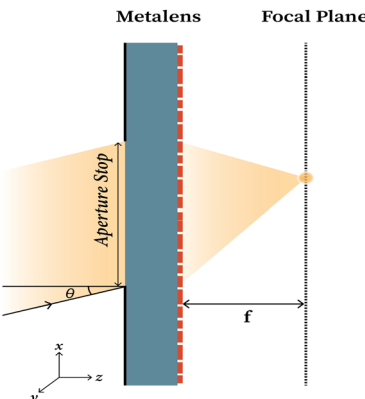


Fig. 12 Schematic illustration of a single layer metalens system consisting of an aperture stop at oblique incidence.

validate the robustness of our approach. To this aim, the GaN-based lens was chosen to meet computational limitations. Single-layer metalenses operate efficiently at normal incidence; however, they experience off-axis aberrations and additional issues at tilted angles, thereby considerably restricting the field of view (FOV) of metalenses.<sup>56</sup> Strategies such as incorporating aperture stops, doublet lenses, or cascaded structural layers are useful in this regard.<sup>57</sup> In this work, as shown in Fig. 12, an aperture stop is positioned at the back of the metalens substrate to restrict incoming light to a specified diameter smaller than that of the lens. Aperture stops with diameters of 5  $\mu\text{m}$ , 10  $\mu\text{m}$ , and 15  $\mu\text{m}$  have been utilized to capture oblique incident light at angles ranging from 1° to 4°. The focal spot intensity, shifts in the focal spot position, FWHM, and focusing efficiency at varying angles and aperture sizes have been analyzed to evaluate lens performance. As shown in Fig. 13(a–c), a noticeable shift in focal spot intensity occurs as the AOI increases from 1° to 4°. Additionally, a reduction in peak intensity is observed with increasing incidence angle. Moreover, as the angle increases, the sidelobes become more prominent. Fig. 13(d and f) show that for aperture stops with a diameter of 5  $\mu\text{m}$  and 15  $\mu\text{m}$ , the focal distance is significantly deviant from the designed focal length. However, it is evident from Fig. 13(e) that for an aperture

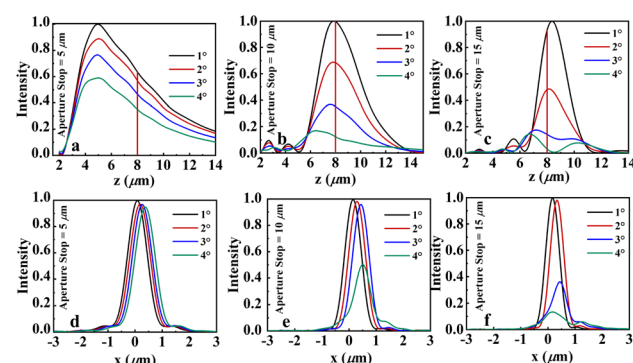


Fig. 13 Normalized intensity plots for GaN metalens along the  $z$  and  $x$ -axes for an aperture stop at (a and d) 5  $\mu\text{m}$ , (b and e) 10  $\mu\text{m}$ , and (c and f) 15  $\mu\text{m}$ . The vertical red line indicates the focal length.



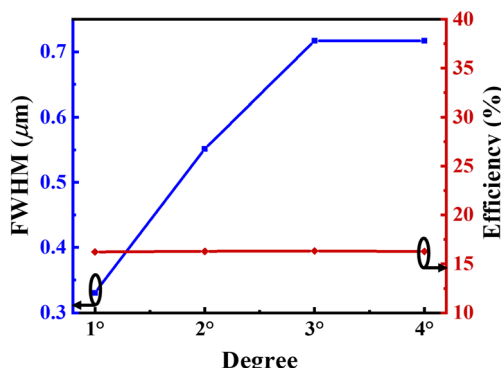


Fig. 14 FWHM and efficiency as a function of the incident angle of the metalens with an aperture stop of 10  $\mu\text{m}$ .

stop with a diameter of 10  $\mu\text{m}$  and incidence angles ranging from 1° to 3° degrees, the focal distance is closely aligned with the designed focal length. Slight deviations are observed as the angle increases. The intensity plots demonstrate that the central lobes are dominant, exhibiting higher intensity than the sidelobes. This configuration results in a narrower FWHM and an efficiency of approximately 16% as shown in Fig. 14. Our findings suggest that, for demonstration purposes, the designed metalens using an 10  $\mu\text{m}$  aperture stop provides reasonable performance.

## 4 Conclusion

We have developed an extensive database on the optical responses of subwavelength-spaced dielectric nanorods through adjusting their corresponding heights and diameters. An efficient transfer learning-based approach is proposed to predict the transmission and phase profile of both GaN and  $\text{TiO}_2$  scatterers. Using this algorithm, our model achieves significantly lower mean squared errors—on the order of  $10^{-6}$  for transmission and  $10^{-5}$  for phase—outperforming existing benchmarks by an order of magnitude. Importantly, the dataset is optimized to satisfy both near-unity transmission and full  $0-2\pi$ . Phase coverage, enabling practical device realization. Performances of the simulated responses of meta-atoms have also been compared and validated with those of the materials experimentally grown on  $\text{SiO}_2$  substrates. Our final contribution was to demonstrate the applications of these nanorods through designing metalenses. Two lenses with 20  $\mu\text{m}$  and 100  $\mu\text{m}$  diameters that ensure reasonable focusing at the intended focal plane have been designed. These miniaturized optical components facilitate the development of portable biomedical optical systems operating in the visible spectrum.

## Author contributions

Adrita Anwar, Shahamat Mustavi Tasin and Khaleda Ali conceived the idea and designed the experiments. Adrita Anwar and Khaleda Ali contributed to writing the main manuscript. Nymul Yeachin and Mahabub Alam Bhuiyan fabricated the  $\text{TiO}_2$  nanorods, performed optical measurements and were involved

in manuscript preparation. Sharnali Islam provided critical feedback and assisted with manuscript editing.

## Conflicts of interest

There are no conflicts to declare.

## Data availability

The datasets generated during this research are available at the GitHub repository: <https://github.com/AdritaAnwar/Metalens-DL-Framework-for-TiO2-GaN-Optical-Property>. For any specific inquiries, please contact Khaleda Ali (khaleda.eee@du.ac.bd).

## Acknowledgements

The authors gratefully acknowledge Mr Mayukh Mallick, M. Sc. student EEE, DU for his valuable contribution in preparing the schematics in the manuscript.

## References

- 1 W. T. Chen, A. Y. Zhu and F. Capasso, *Nat. Rev. Mater.*, 2020, **5**, 604–620.
- 2 M. Pan, Y. Fu, M. Zheng, H. Chen, Y. Zang, H. Duan, Q. Li, M. Qiu and Y. Hu, *Light: Sci. Appl.*, 2022, **11**, 195.
- 3 B. Xu, Z. Huang, X. Guo and S. Li, *IEEE Photonics Technol. Lett.*, 2023, **35**, 61–64.
- 4 S.-J. Kim, C. Kim, Y. Kim, J. Jeong, S. Choi, W. Han, J. Kim and B. Lee, *Sensors*, 2021, **21**, 4584.
- 5 W. T. Chen and F. Capasso, *Appl. Phys. Lett.*, 2021, **118**, 100503.
- 6 M. K. Chen, Y. Wu, L. Feng, Q. Fan, M. Lu, T. Xu and D. P. Tsai, *Adv. Opt. Mater.*, 2021, **9**, 2001414.
- 7 D. Li, M. Gu, C. Li, Y. Tian, B. Fang, J. Wang, Z. Hong and X. Jing, *Precis. Eng.*, 2025, 237–252.
- 8 M. L. Tseng, H.-H. Hsiao, C. H. Chu, M. K. Chen, G. Sun, A.-Q. Liu and D. P. Tsai, *Adv. Opt. Mater.*, 2018, **6**, 1800554.
- 9 X. Zou, G. Zheng, Q. Yuan, W. Zang, R. Chen, T. Li, L. Li, S. Wang, Z. Wang and S. Zhu, *Photonix*, 2020, **1**, 2.
- 10 G.-Y. Lee, J. Sung and B. Lee, *MRS Bull.*, 2020, **45**, 202–209.
- 11 M. Kirlar, E. Aslan, E. Aslan and M. Turkmen, *Optik*, 2023, **290**, 171329.
- 12 J.-S. Park, S. W. D. Lim, A. Amirzhan, H. Kang, K. Karrfalt, D. Kim, J. Leger, A. Urbas, M. Ossiander, Z. Li, *et al.*, *ACS Nano*, 2024, **18**, 3187–3198.
- 13 Z. Liu, D. Wang, H. Gao, M. Li, H. Zhou and C. Zhang, *Adv. Photonics*, 2023, **5**, 034001.
- 14 Y. Han, X. Lu, H. Lv, Z. Mou, C. Zhou, S. Wang and S. Teng, *New J. Phys.*, 2020, **22**, 073021.
- 15 S.-W. Moon, C. Lee, Y. Yang, J. Kim, T. Badloe, C. Jung, G. Yoon and J. Rho, *J. Appl. Phys.*, 2022, **131**, 091101.
- 16 T. Sun, X. Yang, F. Xu and C. Wang, *Nanophotonics*, 2023, **12**, 3243–3255.
- 17 M. Pan, Y. Fu, M. Zheng, H. Chen, Y. Zang, H. Duan, Q. Li, M. Qiu and Y. Hu, *Light: Sci. Appl.*, 2022, **11**, 195.



18 M. Khorasaninejad, A. Y. Zhu, C. Roques-Carmes, W. T. Chen, J. Oh, I. Mishra, R. C. Devlin and F. Capasso, *Nano Lett.*, 2016, **16**, 7229–7234.

19 X. Zhang, Q. Chen, D. Tang, K. Liu, H. Zhang, L. Shi, M. He, Y. Guo and S. Xiao, *Opto-Electron. Adv.*, 2024, **7**, 230126–1.

20 C. Qi, X. He, B. Ren and A. M. Wong, *Adv. Opt. Mater.*, 2024, **12**, 2302459.

21 A. Barulin, Y. Kim, D. K. Oh, J. Jang, H. Park, J. Rho and I. Kim, *Nat. Commun.*, 2024, **15**, 26.

22 M. K. Chen, X. Liu, Y. Sun and D. P. Tsai, *Chem. Rev.*, 2022, **122**, 15356–15413.

23 Y. Chen, Y. Ding, H. Yu and X. Li, *Photonics*, 2024, 249.

24 F. Wang, S. Zhao, Y. Wen, J. Sun and J. Zhou, *Adv. Opt. Mater.*, 2023, **11**, 2300394.

25 J. Lv, R. Zhang, C. Liu, Z. Ge, Q. Gu, F. Feng and G. Si, *Opt. Laser. Technol.*, 2024, **179**, 111396.

26 Q. Zhang, B. Mao, J. Li, X. Xing, D. Zou, Y. Liu, J. Yao, J. Gu, P. Zhu and L. Wu, *Opt. Laser. Technol.*, 2025, **184**, 112550.

27 X.-Q. Jiang, W.-H. Fan, X. Chen, L.-R. Zhao, C. Qin, H. Yan, Q. Wu and P. Ju, *Nanophotonics*, 2025, **14**, 921–934.

28 Y. Hongli, C. Zhaoefeng and L. Xiaotong, *Opt. Express*, 2024, **32**, 15315–15325.

29 F. Wang and X. Shu, *J. Phys. D: Appl. Phys.*, 2023, **56**, 095101.

30 S. Xiao, F. Zhao, D. Wang, J. Weng, Y. Wang, X. He, H. Chen, Z. Zhang, Y. Yu, Z. Zhang, *et al.*, *Opt. Express*, 2023, **31**, 8668–8681.

31 S. An, C. Fowler, B. Zheng, M. Y. Shalaginov, H. Tang, H. Li, L. Zhou, J. Ding, A. M. Agarwal, C. Rivero-Baleine, *et al.*, *ACS Photonics*, 2019, **6**, 3196–3207.

32 I. Tanriover, W. Hadibrata and K. Aydin, *ACS Photonics*, 2020, **7**, 1957–1964.

33 T. Gahlmann and P. Tassin, *Phys. Rev. B*, 2022, **106**, 085408.

34 T. Jahan, T. Dash, S. E. Arman, R. Inum, S. Islam, L. Jamal, A. A. Yanik and A. Habib, *Nanoscale*, 2024, **16**, 16641–16651.

35 M. Decker, W. T. Chen, T. Nobis, A. Y. Zhu, M. Khorasaninejad, Z. Bharwani, F. Capasso and J. Petschulat, *ACS Photonics*, 2019, **6**, 1493–1499.

36 M. Khorasaninejad, W. T. Chen, A. Y. Zhu, J. Oh, R. C. Devlin, C. Roques-Carmes, I. Mishra and F. Capasso, *IEEE J. Sel. Top. Quantum Electron.*, 2017, **23**, 43–58.

37 R. Shi, S. Hu, C. Sun, B. Wang and Q. Cai, *Nanomaterials*, 2022, **12**, 4298.

38 R. Zheng, R. Pan, G. Geng, Q. Jiang, S. Du, L. Huang, C. Gu and J. Li, *Nat. Commun.*, 2022, **13**, 4292.

39 H. Ren, J. Jang, C. Li, A. Aigner, M. Plidschun, J. Kim, J. Rho, M. A. Schmidt and S. A. Maier, *Nat. Commun.*, 2022, **13**, 4183.

40 M. Khorasaninejad and F. Capasso, *Science*, 2017, **358**, eaam8100.

41 W. G. Jacoby, *Elect. Stud.*, 2000, **19**, 577–613.

42 I. Barbeito and R. Cao, *WIREs Comp. Stats.*, 2020, **12**, e1488.

43 W. G. Jacoby, *Elect. Stud.*, 2000, **19**, 577–613.

44 F. Pedregosa, G. Varoquaux, A. Gramfort, V. Michel, B. Thirion, O. Grisel, M. Blondel, P. Prettenhofer, R. Weiss, V. Dubourg, J. Vanderplas, A. Passos, D. Cournapeau, M. Brucher, M. Perrot and E. Duchesnay, *J. Mach. Learn. Res.*, 2011, **12**, 2825–2830.

45 M. Carvalho, A. J. Pinho and S. Brás, *J. Big Data*, 2025, **12**, 71.

46 Y. Jia, C. Qian, Z. Fan, T. Cai, E.-P. Li and H. Chen, *Light: Sci. Appl.*, 2023, **12**, 82.

47 J. Yosinski, J. Clune, Y. Bengio and H. Lipson, *Adv. Neural Inf. Process. Syst.*, 2014, **27**, 3320–3328.

48 Y. Qu, L. Jing, Y. Shen, M. Qiu and M. Soljacic, *ACS Photonics*, 2019, **6**, 1168–1174.

49 A. Agarap, *arXiv*, 2018, preprint, arXiv:1803.08375, DOI: [10.48550/arXiv.1803.08375](https://doi.org/10.48550/arXiv.1803.08375).

50 B. Karlik and A. V. Olgac, *Int. J. Artif. Intell. Expert. Syst.*, 2011, **1**, 111–122.

51 S. Narayan, *Inf. Sci.*, 1997, **99**, 69–82.

52 A. Géron, *Hands-On Machine Learning with Scikit-Learn, Keras, and TensorFlow*, O'Reilly Media, London, United Kingdom, 2nd edn, 2017.

53 E. Bisong and E. Bisong, *Building Machine Learning and Deep Learning Models on Google Cloud Platform: a Comprehensive Guide for Beginners*, 2019, pp. 59–64.

54 D. Berrar, *Cross-validation*, 2019.

55 W. D. Callister Jr, *Fundamentals of Materials Science and Engineering*, John Wiley and Sons, New York, 2001.

56 B. Li, W. Piyawattanametha and Z. Qiu, *Micromachines*, 2019, **10**, 310.

57 S. Li, H.-C. Lin and C. W. Hsu, *Optica*, 2024, **11**, 454–459.

